Evaluating Ground-Penetrating Radar use for water infiltration monitoring

Albane Saintenoy, Sébastien Schneider, Piotr Tucholka

Evaluating Ground-Penetrating Radar use for water infiltration monitoring

Albane Saintenoy, Sébastien Schneider, Piotr Tucholka

Université Paris Sud 11

CNRS

UMR 8148 CNRS-UPS, Laboratoire IDES,

Université Paris Sud 11, Bâtiment 504

91405 Orsay cedex France

Albane.Saintenoy@u-psud.fr

Abstract

Ground-Penetrating Radar (GPR) was tested to monitor water infiltration in sand. Water was injected down an 81 cm long tubed hole, with a piezometer recording the depth of water and a tap valve used to adjust it to 15 cm $\pm$ 2 cm above the bottom of the tube. During the 20 minutes of infiltration a GPR system recorded a trace every second with its transmitter and receiver antennae at a fixed offset position on the surface. The signal, enhanced by differential correction, allows for tracing the evolution of top and bottom limits of the water bulb in space and time. Comparison with hydrodynamic model of the infiltration process and simulated radargrams prove that the GPR reflections trace the wetting front and the saturation bulb. A quantified estimation of the evolution of the top border of the wetting zone is provided.

Index Terms

Ground-Penetrating Radar, water bulb monitoring, interfaces with gradations

I. Introduction

The accurate description and understanding of near-surface water distribution and dynamics are important for effective cleanup of contaminated sites, agricultural issues, and environmental management of water and land resources (Hopmans and Genuchten, 2005). In this

context, an active area of research concerns the local estimation of the hydraulic functions characterizing the vadose zone behavior.

From the hydrology point of view, various designs may be used to measure in situ the hydraulic parameters of an unsaturated soil. One of them is the Triple Ring Infiltrometer at Multiple Suctions (TRIMS) as conceived by Clothier and White (1981) and Perroux and White (1988). While tension infiltrometer experiments provide relatively quick estimates of the hydraulic properties, they can be used only at the soil surface. By comparison, another method based on a modified cone penetrometer, called cone permeameter (Gribb, 1996; Gribb et al., 1998), was designed to inject water under a known pressure into the soil under the surface, usually at a depth around one meter; the cumulative inflow volume and pressure heads at two locations above the source are then measured during the water injection. There are several codes for modeling fluid transports in the ground; among them a finite element modeling code, `HYDRUS`, has been developed by Simunek (1996). Using an inverse code based on HYDRUS (1996), Simunek et al. (1999) and Kodesova et al. (1999) analyzed TRIMS and cone permeameter data via parameter optimization.

From the geophysical point of view, Ground-Penetrating Radar (GPR) is a useful method for investigating near-surface water distribution and dynamics. Indeed, GPR data are highly sensitive to variations of the dielectric permittivity (Saintenoy and Tarantola, 2001), the latter being directly related to the water content, e.g. Ledieu et al. (1986) and Topp et al. (1980). The use of GPR for measuring soil water content is now well established, and reviews of the different existing methods are given by Huisman et al. (2003) and Annan (2005).

Monitoring soil water content variations using GPR has also been attempted to study the hydrological response to an external stimuli such as water infiltration or pumping. In particular, time-lapse GPR surveys allowed for mapping fluid drainage during a pumping test (Tsoflias et al., 2001). Also radar transmission measurements between boreholes have been used to characterize the change in moisture content in unsaturated sandstone due to a controlled water tracer injection (Binley et al., 2001). More recently, joint use of time-lapse cross-borehole transmission GPR travel times and hydrological information from neutron log and infiltration measurements, allowed for the determination of field-scale soil hydraulic parameters (Kowalsky et al., 2005).

The main limitation of GPR use is the medium attenuation which affects the investigation depth. Using borehole antennae, one can characterize the subsurface to a substantial depth but of course limited to the space close to borehole locations. By comparison, off-ground

GPR data can be acquired on large areas with a high spatial resolution and using only the first reflection amplitude variations or the ground wave, the water content variations from the very near-surface can be estimated (Grote et al., 2003; Lambot et al., 2004a; Lambot et al., 2004b; Lambot et al., 2006). Also, in a quite electrically resistive medium like sand, with no magnetic properties, surface-based GPR data can have a penetration depth of at least 10 wavelengths of the sounding wave (typically 1.5 m of penetration using a 800 MHz antenna). In such low attenuating media, many surface-based GPR studies are reported in the literature including in particular 3D reconstruction of the underground heterogeneities (Heincke et al., 2005).

Many GPR data modeling code have been developped (Bergmann et al., 1998; Rejiba et al., 2003; Carcione, 1996; Bourgeois and Smith, 1996; Powers, 1997). In particular the `GprMax` suite of programs, based on finite difference time domain modeling, allows for the simulation of realistic scenarios encountered in everyday use of GPR (Giannopoulos, 2005).

In this paper we address the use of surface-based GPR to detect and monitor the water bulb formation during a water infiltration experiment in sand around 80 cm deep under surface level. We use hydrodynamic numerical modeling to illustrate the water content distribution evolution around the injection point in space and in time. As expected, the transition between unsaturated to saturated medium is gradual, resulting from capillary action in medium to fine sands. We model synthetic GPR data to analyze the GPR response on such a gradual change, and to interpret our field data.

II. Field experiment

The experiment took place in a sand pit nearby Cernay-la-Ville in France. This site is located in Fontainebleau sands of stampian age, a marine facies reworked by wind in upper oligocene with dunes formation (Schneider, 2006). These sands are normally composed of 99 % of quartz. Nine soil samples of known volume were extracted using manual auger every 10 cm down to 80 cm. The laboratory analysis of these samples indicates that their average porosity is 0.43 and the initial moisture content is 0.045 . Their average bulk density is 2.48 $\pm$ 0.03 . A granulometric analysis shows that 10 % of grains have a diameter inferior to 0.125 mm and 86 % inferior to 0.16 mm. These values are typical for Fontainebleau sands.

A 4 cm diameter and 81 cm deep vertical hole was dug with a manual auger and a PVC tube of same length and diameter was placed in the hole. The extremity of a 6 mm hose connected via a tap to a graduated container of 15 l of water was inserted down the hole all

the way to the bottom (Figure 1). During the water injection, the water level at the bottom of the hole was monitored by a piezometer, and manually maintained by the operator at 15 cm $\pm$ 2 cm, using the tap to control the water flow from the water tank down the hose. The cumulated volume of injected water was manually recorded (Figure 2). After a transient phase of infiltration during the first 210 s, a steady-state flow rate was obtained. After 1280 s, the tap was closed and the piezometer indicated that there was no water left in the hole at time $t = 1300\,\mathrm{s}$.

All radar measurements were done using Mala RAMAC system centered on 800 MHz in coplanar Transverse Electric (TE) mode. During the infiltration, GPR data were acquired for tracing in time the effects of water injection, using a static setup of one transmitter and one receiver antennae placed on the surface, respectively 38 cm and 52 cm away from the injection hole (Figure 1). The system was set to acquire a trace every 1.3 s. We kept recording static data until $t = 1730\,\mathrm{s}$.

To characterize the spatial distribution of radar reflections, surface-based GPR traces were also acquired along 34 parallel lines spaced every 3 cm. On each section, 50 traces were recorded, one every 3 cm. Thus a pseudo 3D set of radar data was obtained for a 100 by 150 cm rectangle taking about 20 minutes to record. This data set was acquired twice: before the injection tube installation, and after the water infiltration experiment, at time $t = 1730\,\mathrm{s}$. The difference between the two cubes of data has been used to enhance the variations on GPR data due to the water infiltration.

III. Hydrodynamic modeling

To get an a priori model of the water distribution in space and in time, we simulated the water flow within the geometry of our infiltration experiment. Assuming an homogeneous medium, the system exhibits a radial symmetry around the vertical line centered on the injection hole. Writing the Richards' equation using 3D radial coordinates, no variations in the azimuth angle is considered and the computation reduced to a 2D problem that can be simulated efficiently by `HYDRUS-2D` (Simunek et al., 1996), with the axy-symmetrical vertical flow option turned on.

Our mesh was created on a 1 by 2 m zone. The infiltration occurs at 81 cm depth through a 2 cm radius circular surface with a constant potential head of 15 cm for $0 \leq t \leq 1281\,\mathrm{s}$. The initial conditions are set in pressure head with a linear distribution from $h = -200\,\mathrm{cm}$ at ground level down to $h = -100\,\mathrm{cm}$ at 1 m depth. A free drainage boundary limits the

bottom and no flux is considered through the ground interface and the sides of our domain. After the end of infiltration, the modeling went on for $1281 \leq t \leq 1791\,\mathrm{s}$ to simulate the water redistribution.

The main hydraulic properties of a soil are described by the two relations $K(h)$ and $\theta(h)$ which are, respectively, the hydraulic conductivity and the water content as function of the potential head h. The model of Mualem - van Genuchten (1980) was chosen to describe those two relations. It involves six parameters which are the residual water content θ_r, the saturated water content θ_s, the saturated hydraulic conductivity K_s, the connectivity parameter l, the air entry value parameter α, and the pore size distribution n. The exact values of those parameters for the sand we were doing our infiltration in were not exactly known. We decided to use $\theta_r = 0.045$ and $\theta_s = 0.43$ as estimated from our sample measurements. We took $\alpha = 0.145\,\mathrm{cm}^{-1}$, $n = 2.68$ and $l = 0.5$, which are typical values for a sandy textural soil (Carsel and Parrish, 1988). Schneider (2006) gives $K_s = 0.032\,\mathrm{cm\,s}^{-1}$ as in the range of the saturated hydraulic conductivity for Fontainebleau sands. Let us emphasize again, the idea of this simulation is just to obtain a rough qualitative description of the water distribution in the geometry of our infiltration.

Results of the simulation are presented on Figures 3 and 4. On Figure 3, isolines of $\theta = 0.05$ (plain lines) represent the wetting front at different time steps whereas isolines of $\theta = 0.425$ (dotted lines) delimit the water saturated zone limit. We observe a wetting bulb with an ellipsoidal shape significantly growing with time whereas the water saturated zone stays confined in the vicinity of the injection hole (less than 8 cm). This fact is illustrated in Figure 4 by superposing water content profiles at three different times along the line A-B-C. The volumetric water content θ is converted to relative dielectric permittivity ε_r using the empirical easy-to-use relation proposed by Ledieu (1986). The calculated ε_r varies in the range from 4 to 30.

Simulations with other set of hydraulic parameters show that the shape of the water bulb remains more or less ellipsoidal, depending as expected on the capillarity of the medium. Independently from the exact shape of the water bulb, Figures 3 and 4 allow for defining three regions: the water saturated zone, the unperturbed external zone, and the transition zone in between the two. In all our simulations, the simulated saturated zone always stays very close to the infiltration point when the transition zone wideness is increasing with the infiltration time.

IV. GPR DATA SIMULATIONS

We have used `GprMax2D` (Giannopoulos, 2005) to compute synthetic radargrams. In the present analysis we assumed the electrical conductivity to be sufficiently low that the attenuation of the radar signals through ohmic losses is negligible. We also took the relative magnetic permeability to be equal to 1 in all considered media.

A. Transition zone 1D modeling

The transition from a water unsaturated to a saturated sand presents gradations. Annan et al. (1991) explain that the amplitude of the GPR reflection on such a gradual change depends on the transition thickness to the electromagnetic signal wavelength ratio. Looking for water table is then not always feasible because of the weakness of the reflection as described by Looffler and Bano (2004).

We have simulated surface-based GPR reflections on 1D models presenting a transition zone in between two homogeneous media, as described on Figure 5. The mesh was set to 5 mm by 5 mm in a domain of 3 m by 1.6 m. The computation time step was 9.435^{-12} s. The source waveform is a Ricker centered on 800 MHz. Two cases were considered: in model 1, the transition zone was composed by 25 layers with a 5 mm thickness with a relative dielectric permittivity increase of 1 from one layer to the other. Given the grid step value, this is equivalent to a continuous model. In model 2, the transition zone was made of one homogeneous 12.5 cm thick layer with a relative dielectric permittivity equal to 17.2. This value is such that the time needed for the electromagnetic wave to go through this homogeneous layer is equal to the one to go through the 25 layers of model 1. Other relative dielectric permittivity values were chosen in the range shown on Figure 4.

Supposing a transmitter and a receiver at the surface with a 14 cm offset, Figure 6 shows the comparison between the two simulated traces with model 1 and 2. The gradational transition is creating two reflections, which superpose with the two expected reflections on the two interfaces of the homogeneous transition. Surprisingly, the reflection amplitudes in model 1 are higher than in model 2. Anyway, amplitude modeling is not our goal, as we are only interested in a qualitative description of radargrams. Our simulations allow for using a single intermediate homogeneous layer as a simple but satisfactory model for a transition with gradations.

B. Transition zone 2D modeling

We have created a 2D model with a cylinder of relative permittivity 28, embedded in another cylinder of relative permittivity 15, both cylinders being centered at 81 cm depth in a medium of relative dielectric permittivity 5 (Figure 7). The transmitter and receiver antennae are placed at the surface using the same geometry as presented on Figure 1. Fifteen synthetic traces corresponding to cylinder radius varying from 2 cm to 30 cm are simulated (Figure 8). The inside cylinder (representing the water saturated medium) stays within a radius of 6 cm. Interested only in qualitative results, 2D modeling with guessed parameters is sufficient.

For interpretation needs we have noted interesting features of Figure 8 using alphabet letters from A to E. Corresponding reflecting zones are noted A to D on Figure 7. Reflection A corresponds to the external cylinder interface toward the antennae position. This reflection arrives earlier and earlier while the cylinder radius R linearly increases. Reflection D corresponds to the outer interface of the external cylinder. It arrives later and later while R increases. Reflections B and C correspond to the internal cylinder interfaces. The time delay between those two reflections is constant as expected, as we are keeping the internal cylinder radius to 6 cm. We interpret reflection E as multiple reflections.

The polarity of reflection A is inverse to the polarity of reflection D as expected from reflection coefficent study (Straton, 1941). The same inversion of polarity can be observed on reflections B and C.

Remembering that no gain is applied, Figure 8 clearly shows that the amplitude of reflection D is stronger than that of A; similarly the amplitude of reflection C is stronger than that of B. It results from the combined effect of focalization due to the concavity of the cylinder and of the creeping wave moving along the cylinders surface (Rheinstein, 1968).

V. Field data and their interpretation

A. Static GPR measurements

We processed the raw radar data with residual median filtering (Gerlitz et al., 1993) using a window size corresponding to 150 MHz. Then we subtracted the whole radargram median trace from each trace to highlight differences. The processed radargram is displayed on Figure 9, using no amplitude gain. The vertical glitch at $t = 760\,\mathrm{s}$ corresponds to a small sampling shift in the radar acquisition. This small shift is enhanced by the subtraction of the whole median trace. Apart from this artifact, two reflections appear clearly in these data

and are underlined in gray. The top one is arriving earlier and earlier with the infiltration time (from $t \approx 14\,\mathrm{ns}$ to $t \approx 11\,\mathrm{ns}$). Meanwhile the bottom one is arriving later and later (from $t \approx 18\,\mathrm{ns}$ to $t \approx 25\,\mathrm{ns}$). We relate those two reflections to the ones called A and D on Figure 8, i. e. to the external wetting front evolution.

A zoom on the first 66 s of the static measurements is displayed Figure 10. On this zoom, we have changed the data processing. Instead of subtracting the whole median trace to each trace, we have subtracted the median trace computed on a moving window of 30 traces. This processing highlights better the two interesting reflections at the beginning of the static radargram while their travel times are changing significantly. When the variations in travel time become too weak, this processing removes the reflections we are interested in.

We computed the distance d from the injection point to the reflector responsible for reflection A, using the picked travel time (top gray curve of Figure 9). Lacking a precise zero time measurement we have estimated the crossing point of reflections A and B at the beginning of the infiltration at 14.8 ns $\pm 0.5\,\mathrm{ns}$ (Figure 10). Considering a depth of 81 cm, an apparent velocity is calculated and used to compute the distance d versus the infiltration time (Figure 11). The gap from $t = 131\,\mathrm{s}$ to $t = 262\,\mathrm{s}$ is due to the difficulty of picking reflection A during this interval. Sand layering interfaces could be responsible for interferences. Figure 11 shows a wetting front displacement of 23.5 cm $\pm 2\,\mathrm{cm}$ during the infiltration experiment.

It is more difficult to interpret distance values from reflection D in Figure 9. Indeed, the two-way travel time changes during the infiltration are due to two combined effects: i) the wetting bulb size is increasing, and ii), the wave velocity inside the wetting bulb is decreasing with increasing water content. More information on the behavior of the electromagnetic wave velocity in relation to the differentiated water content is needed for further interpretation.

In Figure 9, between reflections A and D, two reflections could be interpreted as the ones coming from the internal saturated zone, called B and C in Figure 8.

B. GPR data cube

The 100 by 150 cm differential data cube is displayed on Figure 12. This data set confirms the presence of the reflections on the wetting front top and bottom interface (underlined with gray dots). They correspond to reflections A and D, underlined in gray in Figure 9, after $t = 1300\,\mathrm{s}$. Fitting the top points with an hyperbola surface gives a velocity estimation of 0.130 m/ns with an asymptotic standard error of 0.0014 m/ns. The hyperbola surface fitting with latter points gives 0.11 m/ns 0.01 m/ns. This value is less than the above one, as expected

if we consider a wet zone in between the two reflectors (the wave velocity is decreasing as the water content increase).

On Figure 12, traces from the internal saturated zone reflections are not clear. It could be due to the fact that we have acquired the 3D data set too long after the end of the infiltration experiment. We also remark that the injection access tube does not appear in 2D sections nor on static measurements.

VI. Conclusion

We have presented a set of static GPR data acquired during a water infiltration experiment. Repeated recording of one trace from antennae at fixed positions shows two main reflections. From numerical GPR data and hydrodynamic modeling, we interpret those two reflections as coming from the upper and lower interfaces of the wetting front. Static GPR data also display two weaker reflections that we interpret as coming from the upper and lower interfaces of the water saturated zone.

At any time we can compute the distance from the injection point to the wetting front toward the antennae. From this computation we can monitor the displacement of the wetting front as it moves up 23.5 cm between $t = 0\,\mathrm{s}$ to $t = 1450\,\mathrm{s}$, with an estimated accuracy of $\pm 2\,\mathrm{cm}$.

Therefore, surface-based GPR data contain valuable information on the water bulb evolution that could be brought into an inverse hydraulic parameter estimation.

Acknowledgment

We are thankful to A. Zennaki who participated in the acquisition of the data. We are very grateful to the two anonymous reviewers who provided us with highly valuable remarks and suggestions. We would like to acknowledge as well the contribution from A. Giannopoulos for providing the 2D FDTD code. A free version of the software `GprMax2D` may be downloaded from

`http://www.see.ed.ac.uk/~agianno/GprMax/`.

We are also thankful to the `OpenDtect` developers for their 3D data visualization tool (`http://www.opendtect.org`)

and finally, to J. Stockwell for maintaining the `Seismic Unix` package which may be downloaded from `http://www.cwp.mines.edu/cwpcodes/`.

REFERENCES

Annan, A. P., Cosway, S. W., and Redman, J. D., 1991, Water table detection with ground-genetrating radar: Society of Exploration Geophysics technical program expanded abstracts, 494.

Annan, A. P., 2005, GPR method for hydrogeological studies, *in* Rubin, Y., and Hubbard, S., Eds., Hydrogeophysics: Springer New York, 532.

Bergmann, T., Robertsson, J. O., and Holliger, K., 1998, Finite-difference modelling of electromagnetic wave propagation in dispersive medium and attenuating media: Geophysics, **63**, 856–867.

Binley, A., Winship, P., and Middleton, R., 2001, High-resolution characterization of vadose zone dynamics using cross-borehole radar: Water Resources Research, **37**, 2639–2652.

Bourgeois, J. M., and Smith, G. S., 1996, A fully three dimensional simulation for a ground penetrating radar: Fdtd theory compared with experiment: IEEE Transactions on Geosciences and Remote Sensing, **34**, no. 1, 36–44.

Carcione, J. M., 1996, Ground-Penetrating Radar: Wave theory and numerical simulation in lossy anisotropic media: Geophysics, **61**, no. 6, 1664–1677.

Carsel, R. F., and Parrish, R. S., 1988, Developing joint probability distributions of soil water retention characteristics: Water Resources Research, **24**, no. 5, 755–769.

Clothier, B. E., and White, I., 1981, Measurement of sorptivity and soil water diffusivity in the field: Soil Science Society of America Journal, **45**, no. 2, 241–245.

Genuchten, M. T. V., 1980, A closed form equation for predicting the hydraulic conductivity of unsaturated soils: Soil Science Society American Journal, **44**, 892–898.

Gerlitz, K., Knoll, M. D., Cross, G. M., Luzitano, R. D., and Knight, R., 1993, Processing GPR data to improve resolution of near-surface targets: SAGEEP'93 San Diego, CA, Conference proceedings, 561–574.

Giannopoulos, A., 2005, Modelling ground penetrating radar by gprmax: Construction and building materials, **19**, no. 10, 755–762.

Gribb, M. M., Simunek, J., and Leonard, M. F., 1998, Development of cone penetrometer method to determine soil hydraulic properties: Journal of Geotechnical and Geoenvironmental Engineering, **124**, no. 9, 820–829.

Gribb, M. M., 1996, Parameter estimation for determining hydraulic properties of a fine sand from transient flow measurements: Water Ressources Research, **32**, 1965–1974.

Grote, K., Hubbard, S., and Rubin, Y., 2003, Field-scale estimation of volumetric water content using ground-penetrating radar ground wave techniques: Water Resources Research, **39**, no. 11.

Heincke, B., Green, A. G., van der Kruck, J., and Horstmeyer, H., 2005, Acquisition and processing strategies for 3d georadar surveying a region characterized bu rugged topography: Geophysics, **70**, no. 6, 53–61.

Hopmans, J. W., and Genuchten, M. T. V., 2005, Vadose zone: Hydrological processes, *in* Hillel, D., Ed., Encyclopedia of Soils in the Environment: Elsevier Ltd.

Huisman, J. A., Hubbard, S. S., Redman, J. D., and Annan, A. P., 2003, Measuring soil water content with ground-penetrating radar: a review: Vadose Zone Journal, **2**, 476–491.

Kodesova, R., Gribb, M. M., and Simunek, J., 1999, Use of the cone permeameter method to determine soil hydraulic properties, *in* van Genuchten, M. T., and Leij, F. J., Eds., Characterization and measurement of the hydraulic properties of unsaturated porous media: University of California at Riverside.

Kowalsky, M. B., Finsterle, S., Peterson, J., Hubbard, S., Rubin, Y., Majer, E., Ward, A., and Gee, G., 2005, Estimation of field-scale soil hydraulic and dielectric parameters through joint inversion of GPR and hydrological data: Water Resources Research, **41**.

Lambot, S., Antoine, M., van den Bosh, I., Slob, E. C., and Vanclooster, M., 2004a, Electromagnetic inversion of GPR signals and subsequent hydrodynamic inversion to estimate effective vadose zone hydraulic properties: Vadose Zone Journal, **3**, 1072–1081.

——— 2004b, Measuring the soil water content profile of a sandy soil with an off-ground monostatic ground-penetrating radar: Vadose Zone Journal, **3**, 1063–1072.

Lambot, S., Slob, E. C., Vanclooster, M., and Vereecken, H., 2006, Closed loop GPR data inversion for soil hydraulic and electric property determination: Geophysical Research Letter, **33**.

Ledieu, J. P., Clercq, P. D., and Dautrebande, S., 1986, A method of measuring soil moisture by time domain reflectometry: Journal of Hydrology, **88**, 319–328.

Loeffler, O., and Bano, M., 2004, Ground Penetrating Radar measurements in a controlled vadose zone: influence of the water content: Vadose Zone Journal, **3**.

Perroux, K. M., and White, I., 1988, Designs for disc permeameters: Soil Science Society of America journal, **52**, no. 5, 1205–1215.

Powers, M. H., 1997, Modeling frequency-dependent gpr: The Leading Edge, **16**, no. 11, 1657–1662.

Rejiba, F., Camerlynck, C., and Mechler, P., 2003, FDTD-SUPML-ADE simulation for Ground-Penetrating Radar modeling: Radio Science, **38**, no. 1, 1005.

Rheinstein, J., 1968, Backscatter from spheres: A short pulse view: Antennas and Propagation, IEEE, **16**, 89– 97.

Saintenoy, A., and Tarantola, A., 2001, Ground penetrating radar: analysis of point diffractors for modeling and inversion: Geophysics, **66**, 540–550.

Schneider, V., 2006, Stratification et recharge de la nappe des sables de Fontaineblau (bassin de Paris) : contribution de la drainance ascendante depuis la nappe de l'Eocène.: Ph.D. thesis, Université Paris Sud 11.

Simunek, J., and van Genuchten, M. T., 1996, Estimating unsaturated soil hydraulic properties from tension disc infiltrometer data by numerical inversion: Water Resources Research, **9**, 2683–2696.

Simunek, J., Sejna, M., and van Genuchten, M. T., Hydrus-2d, simulation water flow and solute transport in two-dimensional variably saturated media. version 1.0:, Technical report, International Groundwater Modeling Center, Colorado School of Mines, Golden, Colorado, USA, 1996.

Simunek, J., Kodesova, R., Gribb, M. M., and van Genuchten, M. T., 1999, Estimating hysteresis in the soil water retention function from cone permeameter test data: Water Ressources Research, **35**, 1329–1345.

Straton, J. A., 1941, Electromagnetic theory: McGraw Hill, New-York.

Topp, G. C., Davis, J. L., and Annan, A. P., 1980, Electromagnetic determination of soil water content: measurements in coaxial transmission lines: Water Resources Research, **16**, no. 3, 574–582.

Tsoflias, G. P., Halihan, T., and Sharp, J. M., 2001, Monitoring pumping test response in a fractured aquifer using ground-penetrating radar: Water Resources Research, **37**, 1221–1229.

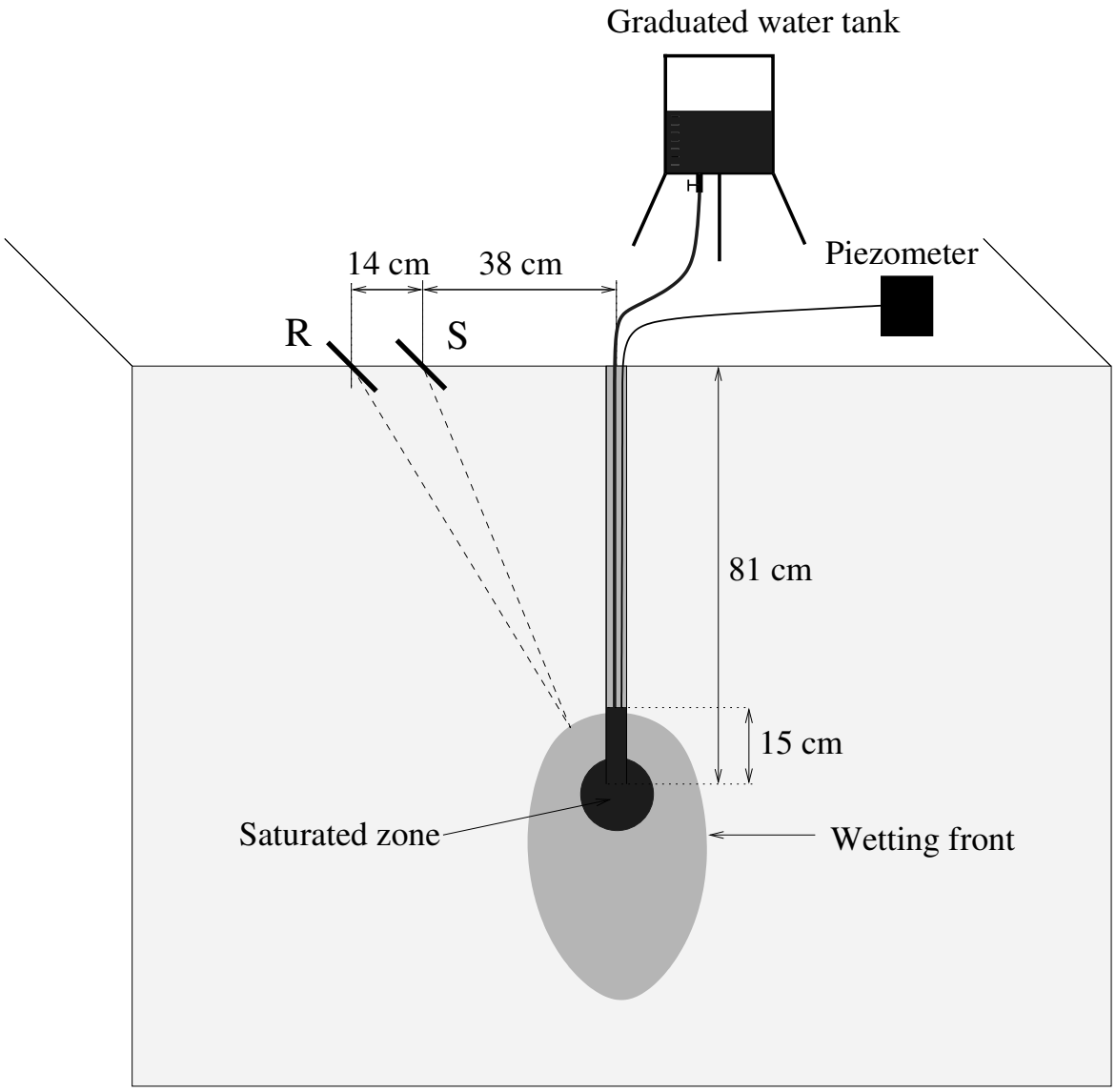

Fig. 1. Experiment setup. Water is injected down the 81 cm long tubed hole while a pair of transmitter and receiver antennae (R, S) is recording a trace every second from the surface. The piezometer records the depth of the water in the tube. A tap regulates the water flux to keep the water level at 66 cm under the surface.

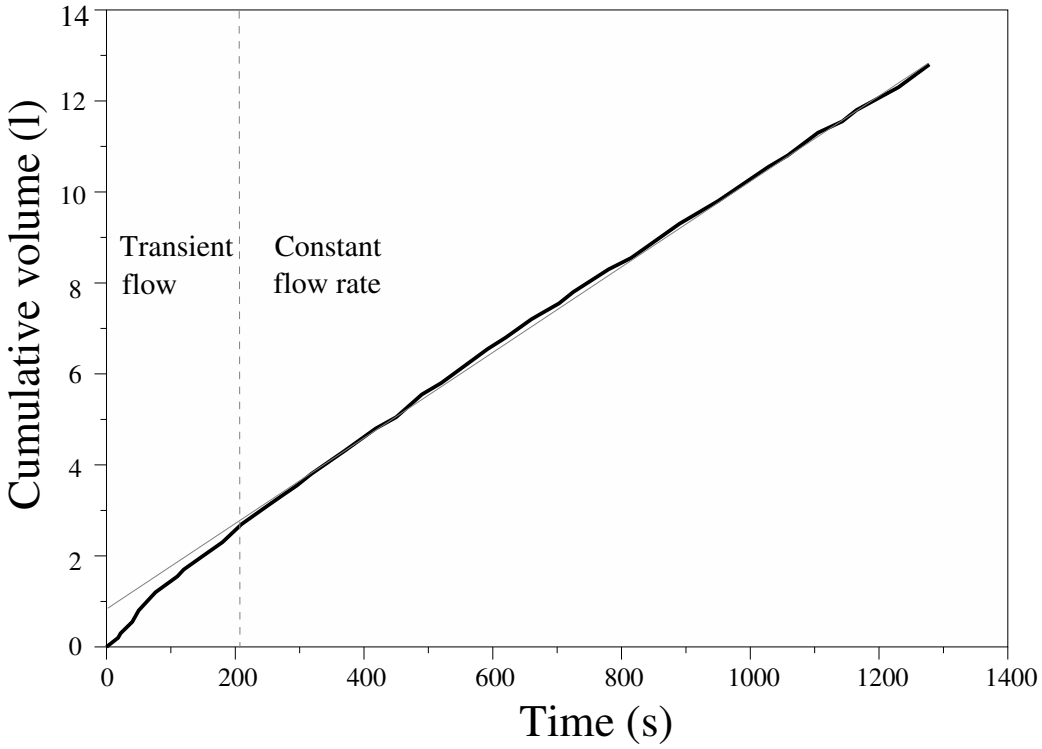

Fig. 2. Cumulative volume of infiltrated water versus time.

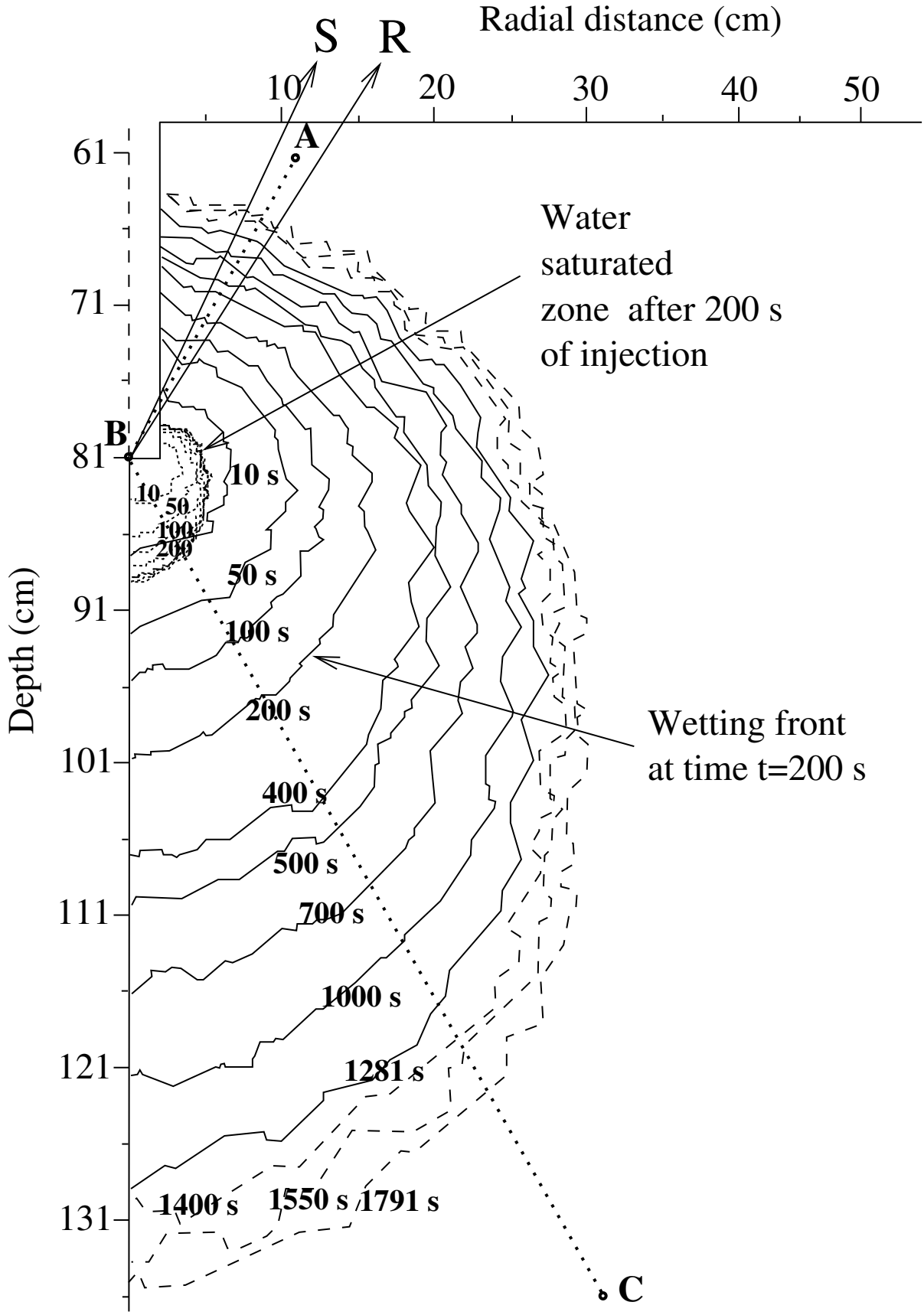

Fig. 3. Snapshots resulting from the HYDRUS-2D modeling. Isolines $\theta = 0.425$ are plotted with dots. Isolines $\theta = 0.05$ are drawn with plain lines during the water injection and dashed lines after stopping the infiltration. Arrows point towards the radar transmitter S and receiver R.

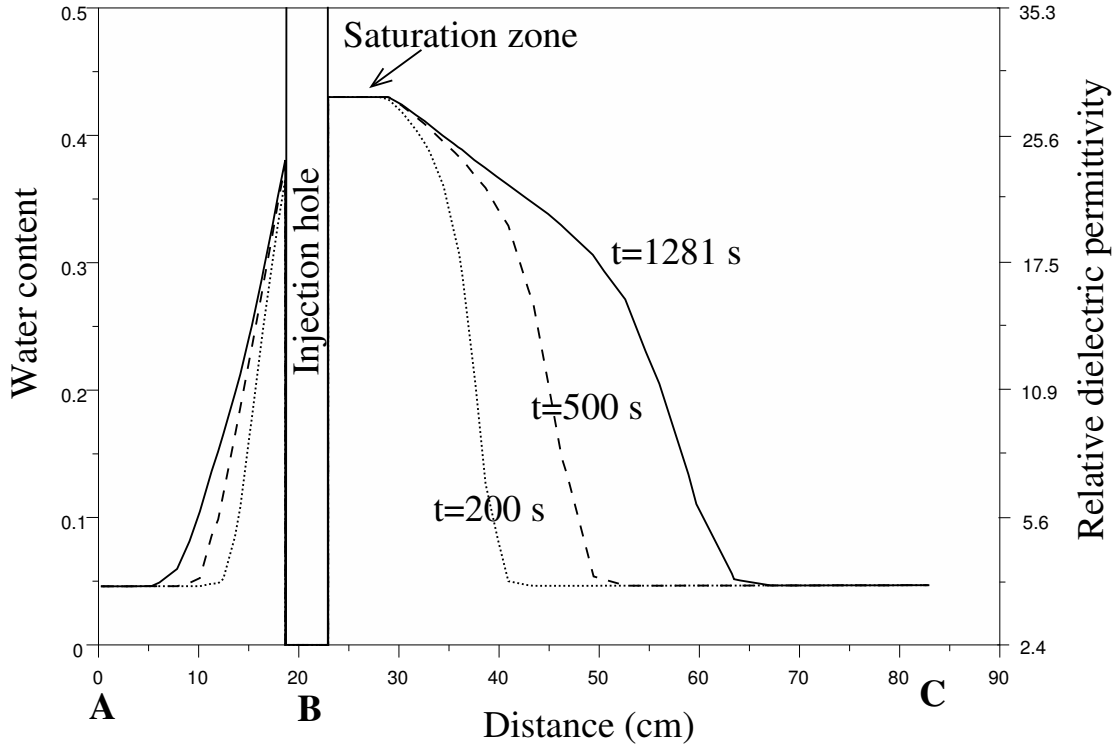

Fig. 4. Water content along the transect A-B-C through the infiltration bulb of Figure 3, at three times.

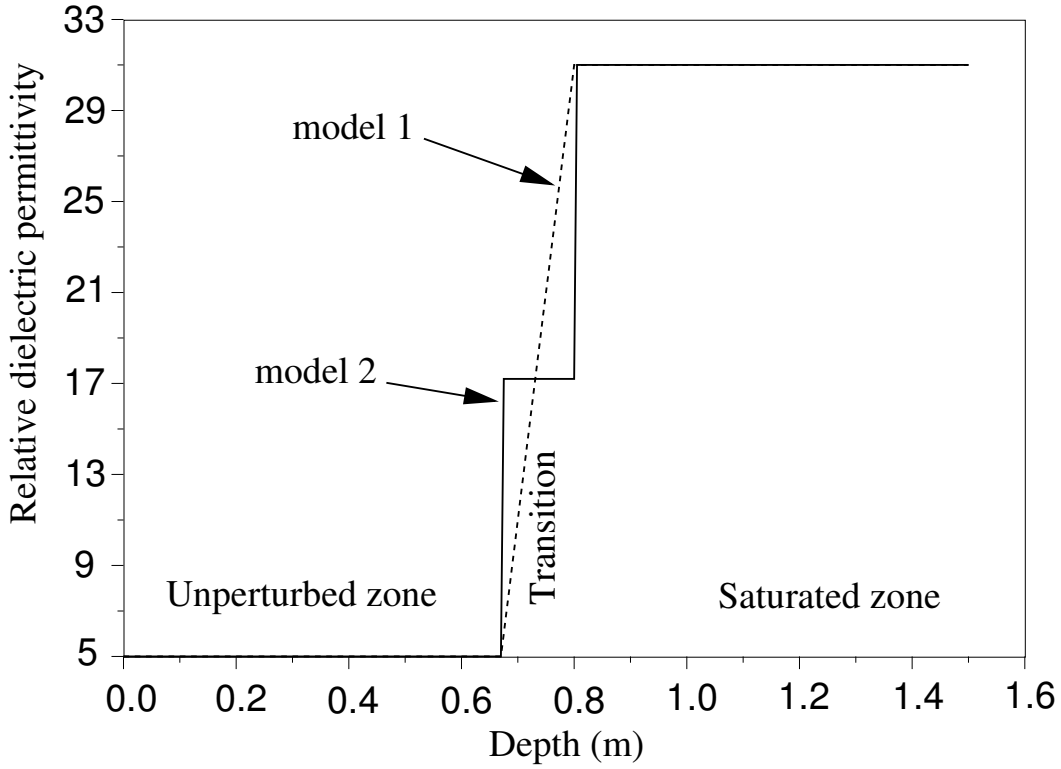

Fig. 5. 1D models created to study the transition zone effect on GPR data. In model 1 (dashed line) the transition zone is made of 25 layers of 5 mm thickness with a relative dielectric permittivity increase from 5 to 31 with a step of 1. In model 2 (plain line), the transition zone consists of a single homogeneous layer of relative dielectric permittivity 17.2 with a thickness of 12.5 cm.

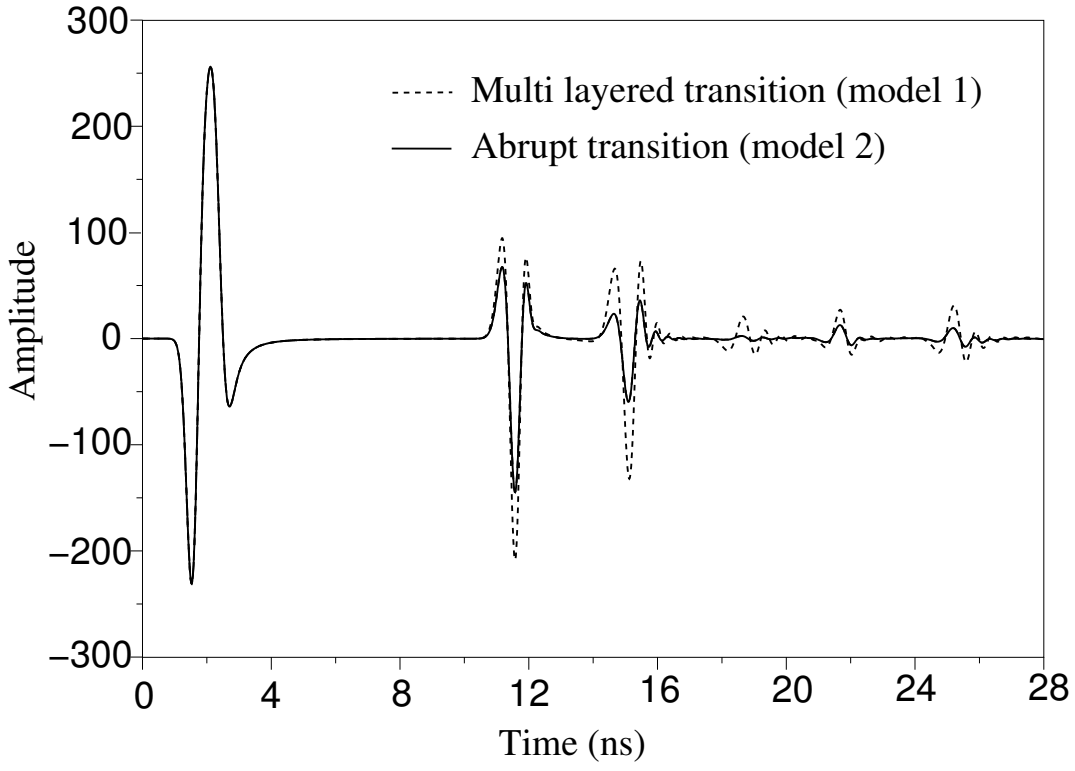

Fig. 6. Simulated traces corresponding to the two models described on Figure 5.

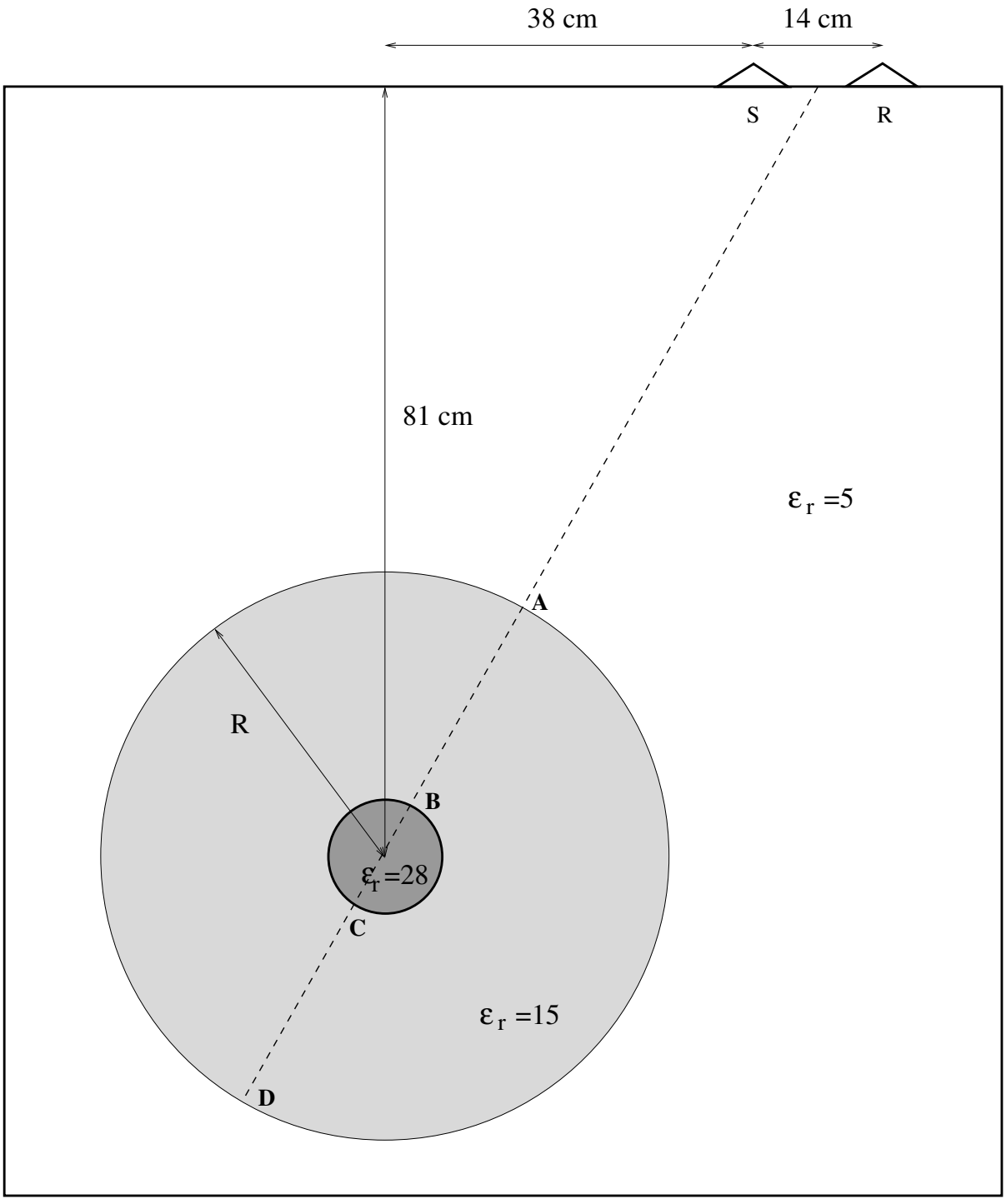

Fig. 7. Model geometry used for GPR data simulations.

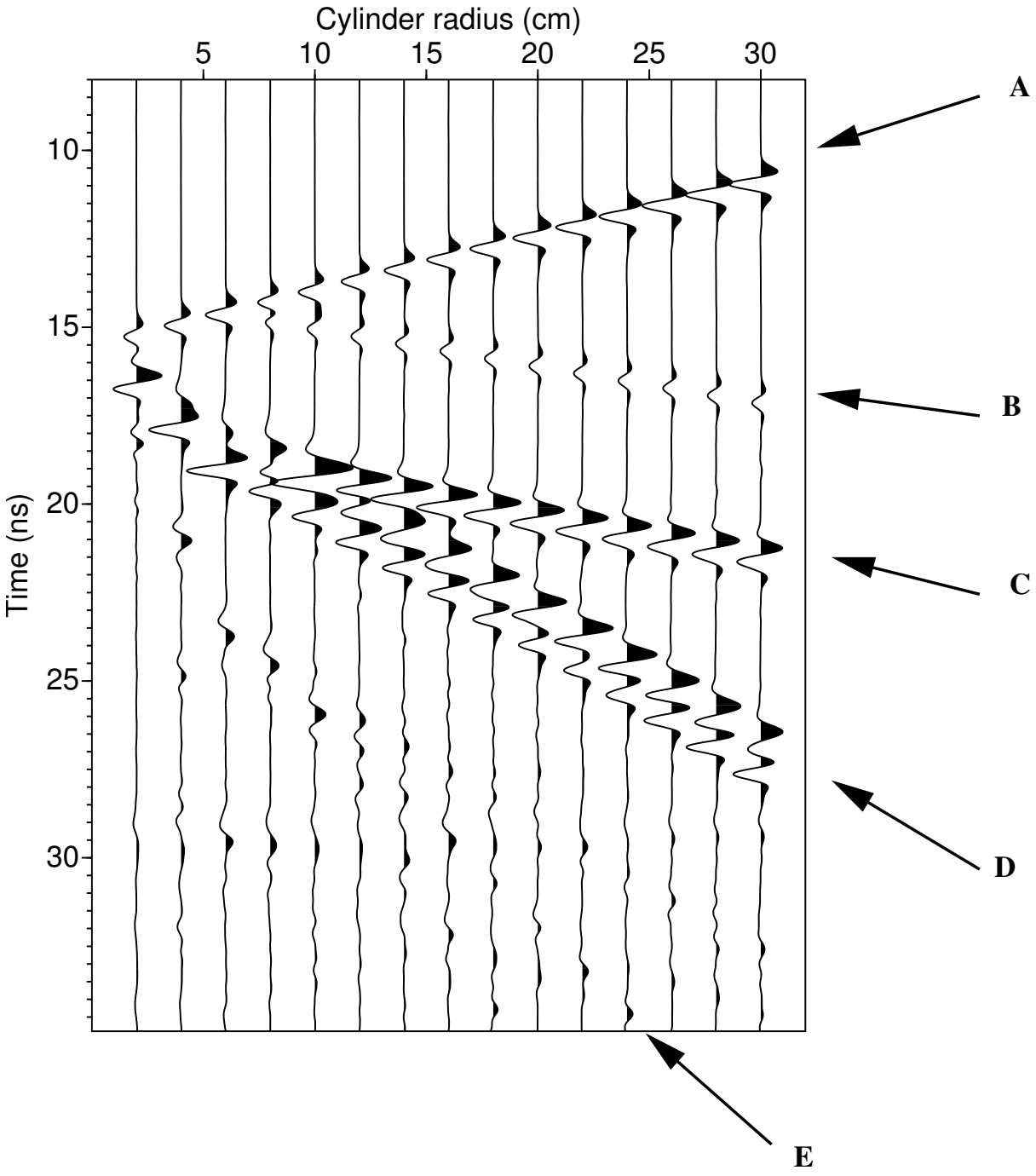

Fig. 8. Simulated traces corresponding to the model described Figure 7. Each trace correspond to a cylinder radius R in the range 2 to 30 cm. No amplitude gain is applied. The main reflections are named from A to E.

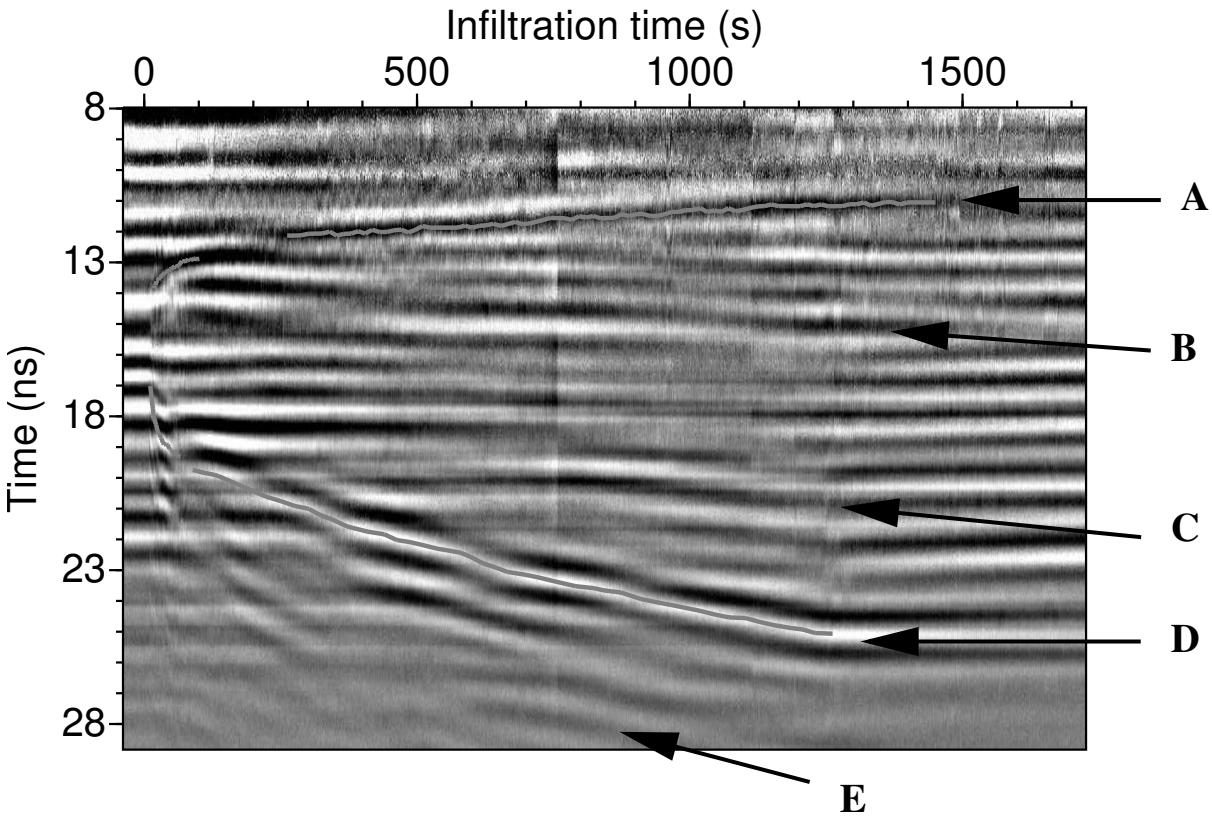

Fig. 9. Recorded traces with fixed antennae during the experiment. The water tap is opened at time 0, closed at time 1280 s and there is no more water at the bottom of the hole at time 1300 s. The data has been band-passed and the whole median trace has been removed from each trace to show up differences. No amplitude gain is applied. Reflections A and D are highlighted by gray lines.

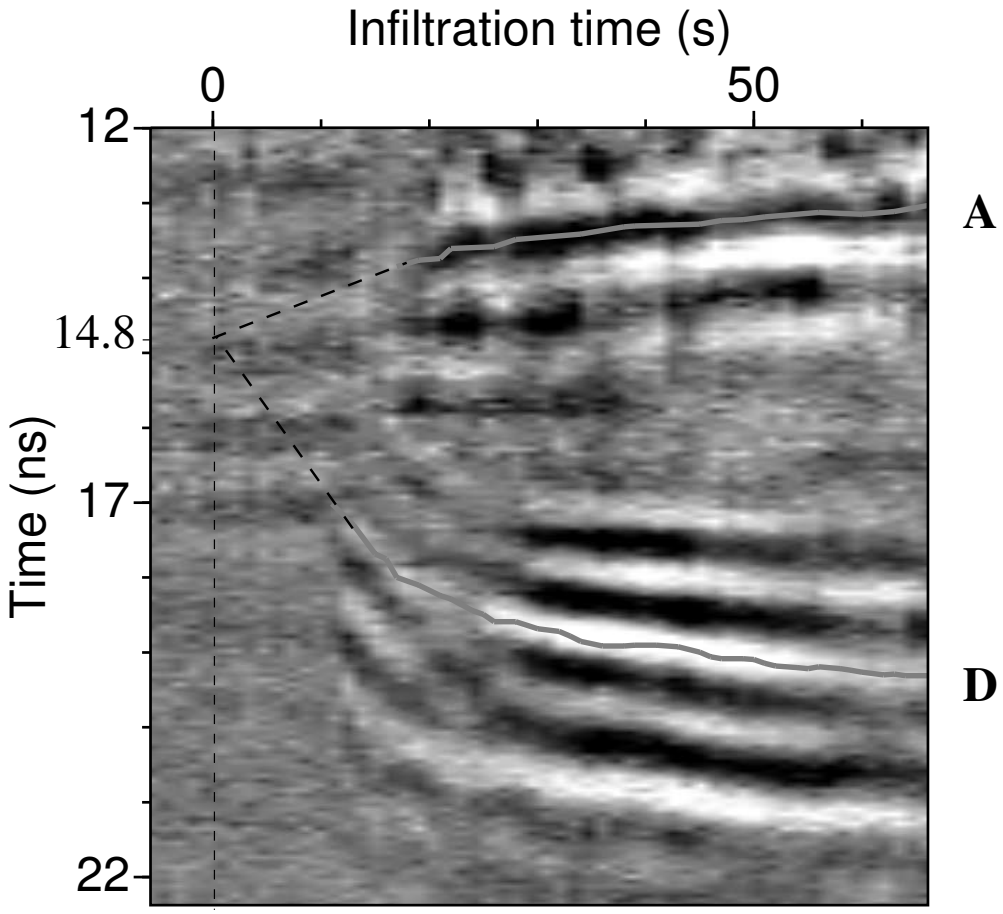

Fig. 10. Zoom of the Figure 9 with a different data processing. The mean of a running 30 trace window is removed from each trace.

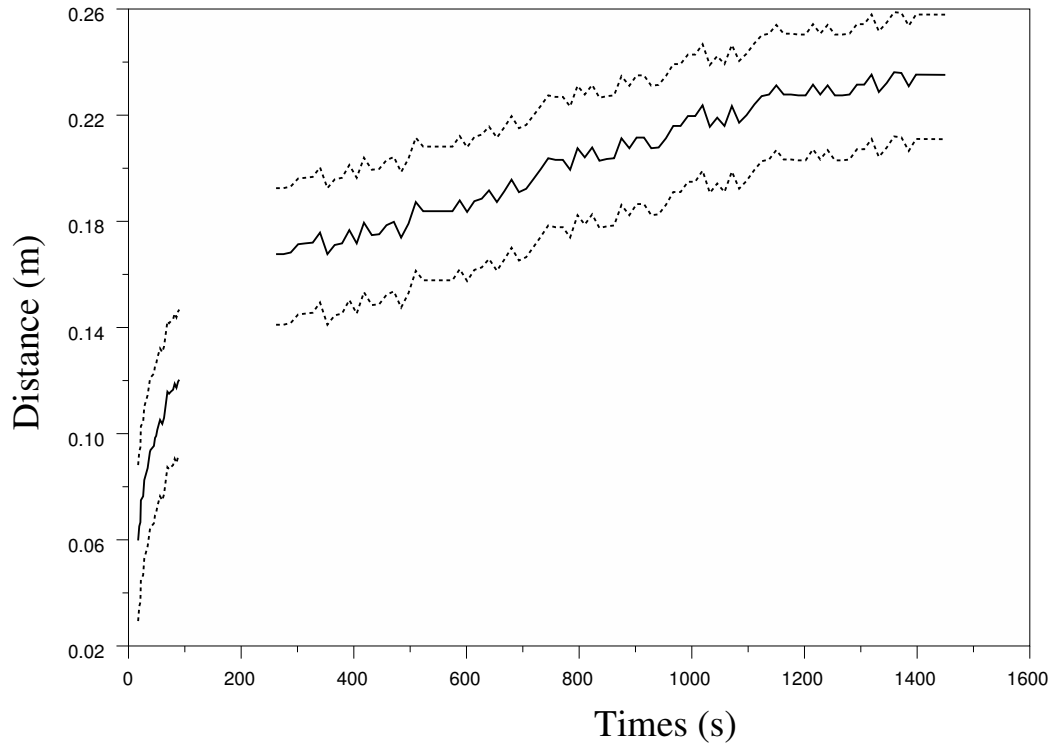

Fig. 11. Distance from the injection point to the wetting front in the antennae direction, with its uncertainty as a function of time, retrieved from picked two-way travel times on reflection A measured on Figure 9.

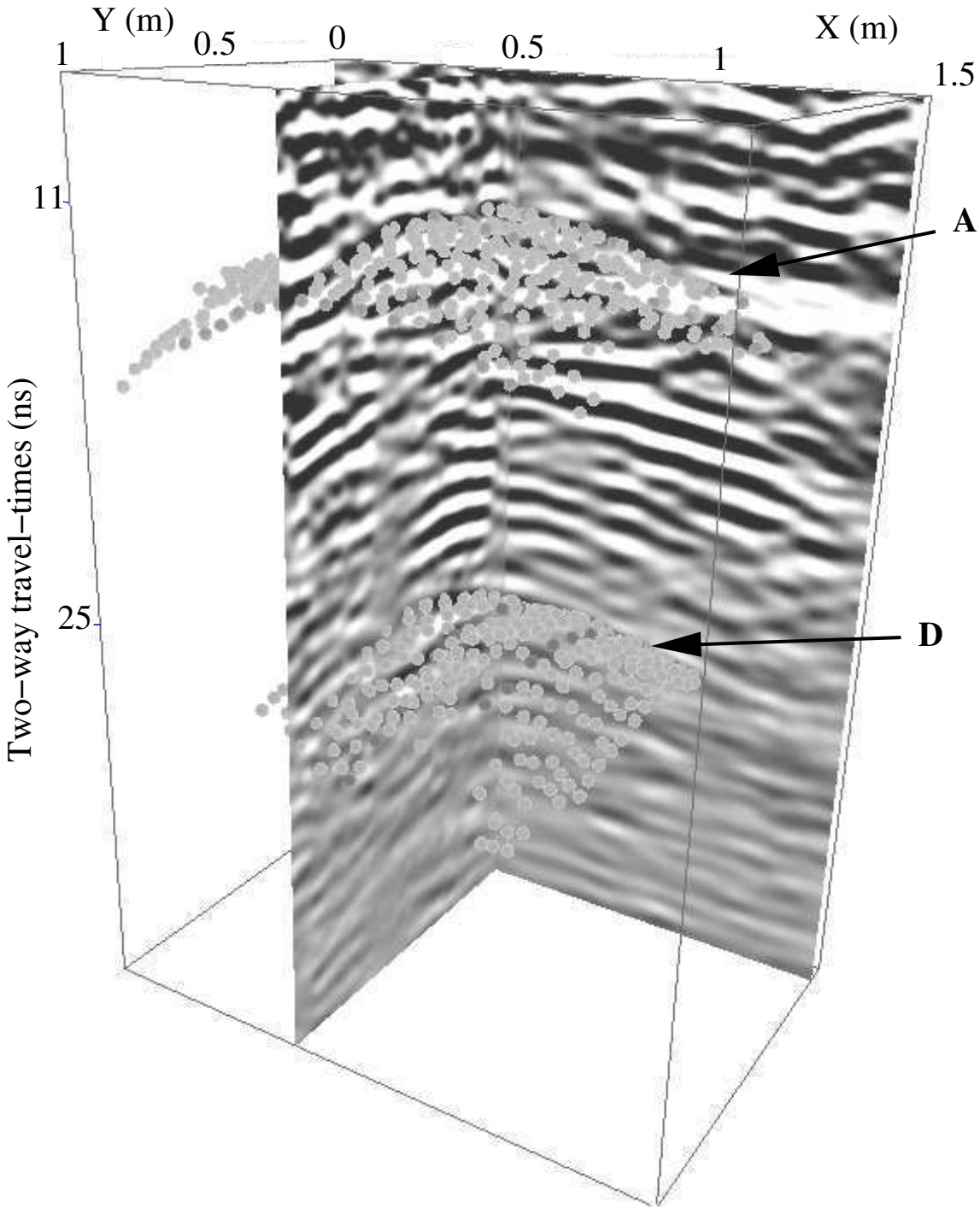

Fig. 12. Cube of surface GPR data obtained by difference between the data sets acquired before and after the water injection. Gray dotted surfaces correspond to the two reflections underlined in gray on Figure 9 after 1300 s.